Progress In Electromagnetics Research B, Vol. 22, 145–170, 2010

QUANTITATIVE ESTIMATION OF SCATTERING WAVES IN CYLINDER-BODY MODEL FOR BODY AREA NETWORKS: COMPARISON OF ANALYSES WITH UNIFROM CYLINDER- AND SLAB-BODY MODELS

C. Y. Seo

Graduate School of Science and Technology
Chiba University
1-33 Yayoi-cho, Inage-ku, Chiba-shi 263-8522, Japan

K. Saito and M. Takahashi

Research Center for Frontier Medical Engineering
Chiba University
1-33 Yayoi-cho, Inage-ku, Chiba-shi 263-8522, Japan

K. Ito

Graduate School of Engineering
Chiba University
1-33 Yayoi-cho, Inage-ku, Chiba-shi 263-8522, Japan

Abstract—This paper estimates separately the components of scattering waves generated in cylinder-body model for body area networks. For the evaluation, scattering field formulations in relation to uniform cylinder- and slab-body models are provided, and the reliability of the analyses is testified by the comparison with results computed by the finite-difference time-domain (FDTD) method. Creeping waves, cylinder leaky waves, and cylinder guided waves, which are created only in cylindrical structure, are extracted quantitatively by contrasting the scattering waves that are calculated with the two body models. In addition to the extracted waves, other components of scattering waves such as reflected waves, transmitted waves, surface waves, leaky waves, and guided waves also are examined. From evaluations with various operating frequencies and thicknesses of the body model, it is confirmed that reflected waves have the most influence on electrical characteristics of a source. Moreover creeping

Corresponding author: C. Y. Seo (ChangYong_SEO@graduate.chiba-u.jp).

waves and cylinder leaky waves are generally dominant at the opposite side of the cylinder when a source is located near cylinder surface. Furthermore, the existence of creeping waves with low attenuation in the vicinity of cylinder surface is demonstrated by electric field intensities calculated by varying the observation point along cylinder axis.

1. INTRODUCTION

The grafting of wireless communications onto the human body has been conceptualized from a few decades ago [1, 2]. At present due to rapid technological developments, there have been recent and novel applications of wireless communications such as telemedicine, smart home, and wireless identification system [3, 4]. As a result of new communication networks that operate in body-centric environments, body area networks (BANs) have been introduced; with a great number of the papers being published on the subject. The current research for BANs can be separated into three main groups: those which focus on the development of antennas for implant or wearable devices [5–7]; those which research the channel model with respect to body postures or consider the effect of multi-path propagations by other objects in a restricted interior space [8–10]; and finally those that examine the propagation characteristics in the vicinity of the human body or inside the human body through the specific absorption rate (SAR) [11–13]. However, most of papers are limited in the explanation of scattering waves because of the evaluation method by the FDTD method or physical experiments that provide total field results only, although analytical solutions for scattering problem in the inhomogeneous environment between the free space and the human body may be useful for the design of antennas considering the characteristics changed by the human body or for the effectual estimation of communication channels in BANs.

For theoretical analysis, it is inevitable that the human body needs to be simplified, thus planar and circular-cylinder structures have been used to create a representation of the human body. The analysis with three-layered half-space geometry substituted for the half-space of the human body was examined [14], and the propagation on the model, especially about surface wave modes, was investigated [15]. In order to approach the finite body, circular-cylinder geometry similar to sectional parts of the human body, such as arms, legs, and torso, was employed and the propagation characteristics including scattering waves were evaluated in relation to the transverse section of the human body [16].

The fields due to a finite source in the presence of a dielectric

material are distributed not only by the reflection and transmission but also by specific physical propagations depending on a shape of the dielectric. The individual interpretation of such propagations has been a matter of great interest in radio wave propagation, and the consideration and application of it are important factors in the design of antennas. In particular, the separate evaluation of propagating waves in BANs of which the human body is located in the center of analysis environment may assist the concrete comprehension of scattering characteristics by the human body.

In this paper, when the human body is simplified to a lossy-dielectric infinite circular cylinder, specific cylinder waves generated by the cylindrical geometry are investigated quantitatively. The method of estimation is accomplished by comparing the results calculated with circular-cylinder and planar-slab structures. Besides reflected waves (RWs) and transmitted waves (TWs), the slab supports leaky waves (LWs), surface waves (SWs), and guided waves (GWs). The cylinder supports creeping waves (CWs), and in addition, cylinder LWs (CLWs), cylinder SWs (CSWs), and cylinder GWs (CGWs). In general, the evaluations of LWs, SWs, CWs, CLWs, and CSWs are conducted with poles, where the denominator of integrand in analytical solutions is zero, in a complex plane. In case of slab, it can be acquired from reflection and transmission coefficients, and a cylinder is from overall integrand of field formulation [17, 18]. However, it is hard to examine universally for BANs with such analyses because poles have to be recalculated if any one variable in several calculation conditions is changed. Moreover, since the analyses are accompanied by fundamental conditions for asymptotic evaluation, errorless results in short range communications cannot be expected [16]. Therefore, the consideration for BANs with a few meters range should be supported with an exact numerical analysis. In this paper, the estimations of the scattering modes including the CW, CLW, and CGW modes in the near-field region of BANs are performed based on results computed numerically.

This paper is constructed as follows. Section 2 describes the propagating waves in circular-cylinder and planar-slab structures in detail and explains about the method of quantitative estimation of CWs, CLWs, and CGWs. The scattering electric field formulations inside and outside of the cylinder and analytical solutions for the slab are derived in Section 3. In Section 4.1, firstly, in order to confirm the reliabilities of the formulations in Section 3, with a finite linear dipole and the 2/3-muscle equivalent tissue as the human body, the numerical result accomplished with the analytical solutions is compared with the result calculated by the FDTD method. Secondly, the distribution of

the specific cylinder waves extracted by the subtraction of scattering results in cylinder- and slab-body models is exhibited and discussed. In Section 4.2, the results obtained with the variations of radius of cylinder-body model and operating frequency are presented and general characteristics of scattering waves in cylinder-body model for BANs are discussed separately. Finally, Section 5 summarizes results and conclusions.

2. WAVES IN STRUCTURES OF CIRCULAR CYLINDER AND PLANAR SLAB

Figure 1 illustrates the wave modes generated by a circular-cylinder dielectric when a source is located outside the dielectric. The SW, LW, and GW modes are observed in the longitudinal plane, and the CW, CSW, CLW, and CGW modes are associated with the transverse plane. With the term "creeping waves" usually used to describe all types of azimuthally propagating waves on a cylinder [18], the CW mode in this paper terminologically contains the CSW mode also. The propagation behaviors of CLWs and CGWs are analogous to LWs and GWs, but the difference between the waves is to be generated in connection with the longitudinal and azimuthal boundaries of the cylinder, respectively. The waves described in Figure 1(b) propagate in precisely toward the longitudinal direction simultaneously with the azimuthal direction. Such all waves including RWs and TWs are designated collectively as scattering waves.

When the outside and inside of the cylinder are assigned as regions

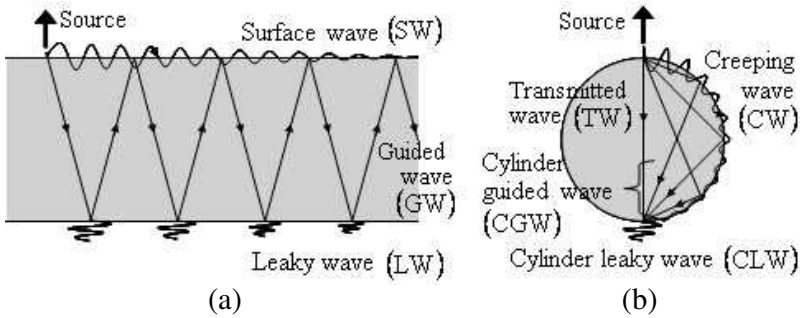

Figure 1. Propagating waves in a circular-cylinder structure. RWs in the illuminated region exist additionally. LWs and CLWs are distributed on overall cylinder surface. (a) In longitudinal section. (b) In transverse section.

1 and 2, respectively, the electric fields in each region emanated from a source located in region 1 are expressible as written in (1) and (2). The notation $\mathbf{E}^{(ij)}$ is adopted when field point is in region i and source point is in region j. The superscripts 0 and S mean the incidence in the free space of region 1 and the scattering, respectively. In (1), the RW mode is for the optically illuminated area. In non-illuminated zone, the TW mode which has the shortest propagating path is corresponded and the SW mode is excluded.

$$\begin{aligned}\mathbf{E}^{(11)\_C} &= \mathbf{E}^0 + \mathbf{E}^{S(11)\_C} \\ &= \mathbf{E}^0 + \mathbf{E}^{RW}\left(\text{or } \mathbf{E}^{TW}\right) + \mathbf{E}^{SW}(\text{or } 0) + \mathbf{E}^{LW} + \mathbf{E}^{CLW} + \mathbf{E}^{CW} \quad (1)\end{aligned}$$

$$\mathbf{E}^{(21)\_C} = \mathbf{E}^{S(21)\_C} = \mathbf{E}^{GW} + \mathbf{E}^{CGW} \quad (2)$$

In case of a dielectric with the structure of infinite planar slab, since any longitudinal section of the slab makes the identical plane with Figure 1(a), the longitudinal propagation modes shown in Figure 1(a) are formed. Unlike the cylinder structure, the analysis region for the slab is split into three: source region, slab region, opposite region of source. The illuminated area is the source region, and the TW mode is supported only in other two regions. When the regions are numbered as regions 1, 2, and 3, respectively, (3)–(5) explain the wave modes in each region.

$$\mathbf{E}^{(11)\_P} = \mathbf{E}^0 + \mathbf{E}^{S(11)\_P} = \mathbf{E}^0 + \mathbf{E}^{RW} + \mathbf{E}^{SW} + \mathbf{E}^{LW} \quad (3)$$

$$\mathbf{E}^{(21)\_P} = \mathbf{E}^{S(21)\_P} = \mathbf{E}^{TW(21)} = \mathbf{E}^{GW} \quad (4)$$

$$\mathbf{E}^{(31)\_P} = \mathbf{E}^{S(31)\_P} = \mathbf{E}^{TW(31)} + \mathbf{E}^{LW} \quad (5)$$

When slab thickness is equal to cylinder diameter, the longitudinal section cutting across the center of cylinder is same geometrically with it of the slab. The fields on this observation plane as a criterion plane were evaluated for the investigation of propagation characteristics in BANs [14–16]. On this common plane, the specifically propagating waves (CWs, CLWs, and CGWs) created only in cylinder structure can be extracted by the subtraction of scattering waves calculated with cylinder and slab. By the relations between (1) and (3), and between (1) and (5), CWs and CLWs in source region and opposite region of source, respectively, are calculated. For CGWs inner cylinder, (2) and (4) are applied.

3. SCATTERING ELECTRIC FIELD FORMULATIONS

The field formulation entirely depends on source direction. As representative source directions in connection with cylinder coordinates, it

can be divided into two types: a vertical electric dipole (VED) to cylinder surface and a horizontal electric dipole (HED) parallel to cylinder axis If cylinder axis and source direction are identical, the analysis has the homogeneous environment in regard to that direction. In this case, it is difficult to expect the specific scattering waves because the waves are caused by an inhomogeneous environment This paper, therefore, deals with a VED case as a source for a fundamental examination. In this paper, a time-harmonic convention of $e^{j\omega t}$ with angular frequency ω is assumed and suppressed.

3.1. Circular-cylinder Structure

As the geometry for analysis, Figure 2 shows the human body represented with a lossy-dielectric infinite circular cylinder of radius a in the free space. The human body has the electrical properties of conductivity σ and relative permittivity ε_r in accordance with operating frequency. The permittivity and permeability of the free space are ε_0 and μ_0, respectively. The wavenumbers in regions 1 and 2 are respectively k_1 and k_2.

The scattering problems having boundaries which coincide with cylindrical coordinate surfaces are firstly constructed from the solutions satisfying the homogeneous scalar Helmholtz equation in cylindrical coordinate system. The solutions can be obtained by the method of separation of variables. Linear combinations of the solutions are also solutions to the Helmholtz equation, and these can be expressed by the discrete summation over eigenvalue of constant n relative to only ϕ-domain and the integration over eigenvalue of k_z, which is the wavenumber of z-direction irrespective of regions in

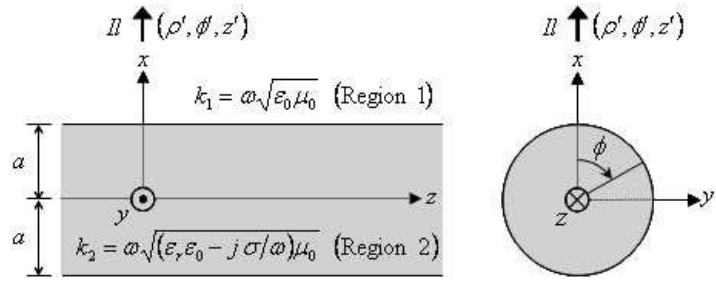

Figure 2. Geometry for analysis of circular-cylinder model. Source with current moment Il is located at (ρ', ϕ', z') in region 1 of the free space. Region 2 with shading indicates the human body. (a) Longitudinal section. (b) Transverse section.

Figure 2 [19, 20]. The eigenfunction for any values of such eigenvalues is solved explicitly by imposing boundary conditions at the interface $\rho = a$ between the cylinder and the free space [21, 22]. Through such a procedure for the eigenfunction solutions, when a VED with current moment Il is located at (ρ', ϕ', z'), scattering electric field formulations at observation point (ρ, ϕ, z) in region 1 are derived as written in (6)–(8).

$$E_\rho^{S(11)\text{-}C} = -\frac{Il\omega\mu_0}{8\pi}\int_{-\infty}^{\infty} dk_z \sum_{n=0}^{\infty} \frac{(2-\delta_0)}{k_{\rho 1}^2} \cos\left(n\left(\phi-\phi'\right)\right) e^{-jk_z(z-z')}$$
$$\times \left[\left\{A_1 \frac{n}{\rho} H_n^{(2)}\left(k_{\rho 1}\rho\right) + B_1 \frac{jk_z}{k_1} \frac{\partial H_n^{(2)}\left(k_{\rho 1}\rho\right)}{\partial \rho}\right\} P\left(k_{\rho 1}, n, k_z; \rho'\right)\right.$$
$$\left. + \left\{C_1 \frac{jk_z}{k_1} \frac{\partial H_n^{(2)}\left(k_{\rho 1}\rho\right)}{\partial \rho} - D_1 \frac{n}{\rho} H_n^{(2)}\left(k_{\rho 1}\rho\right)\right\} Q\left(k_{\rho 1}, n, k_z; \rho'\right)\right] \quad (6)$$

$$E_\phi^{S(11)\text{-}C} = -\frac{Il\omega\mu_0}{8\pi}\int_{-\infty}^{\infty} dk_z \sum_{n=0}^{\infty} \frac{(2-\delta_0)}{k_{\rho 1}^2} \sin\left(n\left(\phi-\phi'\right)\right)\ e^{-jk_z(z-z')}$$
$$\times \left[\left\{-A_1 \frac{\partial H_n^{(2)}\left(k_{\rho 1}\rho\right)}{\partial \rho} - B_1 \frac{jnk_z}{k_1\rho} H_n^{(2)}\left(k_{\rho 1}\rho\right)\right\} P\left(k_{\rho 1}, n, k_z; \rho'\right)\right.$$
$$\left. + \left\{-C_1 \frac{jnk_z}{k_1\rho} H_n^{(2)}\left(k_{\rho 1}\rho\right) + D_1 \frac{\partial H_n^{(2)}\left(k_{\rho 1}\rho\right)}{\partial \rho}\right\} Q\left(k_{\rho 1}, n, k_z; \rho'\right)\right] \quad (7)$$

$$E_z^{S(11)\text{-}C} = -\frac{Il\omega\mu_0}{8\pi}\int_{-\infty}^{\infty} dk_z \sum_{n=0}^{\infty} \frac{(2-\delta_0)}{k_{\rho 1}^2} \cos\left(n\left(\phi-\phi'\right)\right) e^{-jk_z(z-z')}$$
$$\times \left[\left\{-B_1 \frac{k_{\rho 1}^2}{k_1} H_n^{(2)}\left(k_{\rho 1}\rho\right)\right\} P\left(k_{\rho 1}, n, k_z; \rho'\right)\right.$$
$$\left. + \left\{-C_1 \frac{k_{\rho 1}^2}{k_1} H_n^{(2)}\left(k_{\rho 1}\rho\right)\right\} Q\left(k_{\rho 1}, n, k_z; \rho'\right)\right] \quad (8)$$

where

$$P\left(k_{\rho 1}, n, k_z; \rho'\right) = \frac{n}{\rho'} H_n^{(2)}\left(k_{\rho 1}\rho'\right) \quad (9)$$

$$Q\left(k_{\rho 1}, n, k_z; \rho'\right) = -\frac{jk_z}{k_1} \frac{\partial H_n^{(2)}\left(k_{\rho 1}\rho'\right)}{\partial \rho} \quad (10)$$

δ_0 is the Kronecker delta function, which is 1 if $n = 0$, and 0 otherwise. $k_{\rho 1} = -\sqrt{k_1^2 - k_z^2}$ and $H_n^{(2)}(x)$ is the Hankel function of the second

kind of order n. The coefficients A_1, B_1, C_1, and D_1 deduced from boundary conditions are explained in the Appendix A. The expressions in square brackets in (6)–(8) are organized individually with the functions corresponding to observation point and the functions of source points as written in (9) and (10).

Field formulations of $\mathbf{E}^{S(21)}$ for observation point inner cylinder is attained basically by altering the variables associated with region 1 in braces in (6)–(8) into the variables in region 2. Furthermore, the Bessel function should be substituted for the Hankel function because the radiation condition at the origin where $\rho = 0$ has to be satisfied. Namely, the variables A_1, B_1, C_1, D_1, k_1, $k_{\rho 1}$, and the function $H_n^{(2)}(k_{\rho 1}\rho)$ in braces are respectively changed into a_2, b_2, c_2, d_2, k_2, $k_{\rho 2}$, and $J_n(k_{\rho 2}\rho)$. $k_{\rho 2} = -\sqrt{k_2^2 - k_z^2}$, $J_n(x)$ is the Bessel function of the first kind of order n, and the coefficients a_2, b_2, c_2, and d_2 from boundary conditions in relation to region 2 are also described in the Appendix A.

3.2. Planar-slab Structure

Figure 3(a) shows the human body regarded as a lossy-dielectric infinite planar slab of thickness $2a$ in the free space. By the same set of coordinates with the longitudinal section of circular-cylinder model the geometry for analysis in this section is identical with Figure 2(a) except for the addition of region 3 which is the opposite region of source The symbols in Figure 3(a) are the same meanings with them in Figure 2(a).

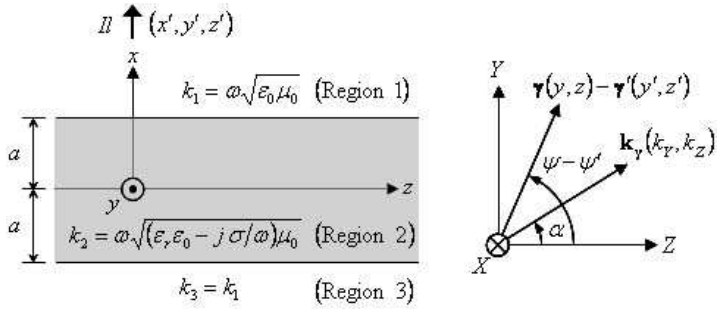

Figure 3. (a) Geometry for analysis of planar-slab model. Source with current moment Il is located at (x', y', z') in region 1 of the free space. Region 2 is the human body. (b) In XYZ coordinates with the origin moved into source coordinates, observation vector $\boldsymbol{\gamma}$ and wavenumber vector $\mathbf{k}_\gamma$ involved with Y and Z coordinates.

The analytical solutions for a dielectric planar slab can be established by the use of the Fresnel reflection and transmission coefficients in a multilayered medium [20] or by the eigenfunction expansion of the dyadic Green's functions associated with planar stratified media [21]. However, since the former is developed by the generalized reflection coefficient which implicates the series of multiple reflections inner dielectric, the field formulations for each region have complex forms In the latter case, the discrete summation over eigenvalue of constant n relative to the ϕ-domain is also contained, and therefore the calculation time is slow due to its convergence.

In this paper, in order to formulate scattering electric fields with simple expressions, the perfect electric conductor (PEC) and perfect magnetic conductor (PMC) placed virtually at the middle of inner slab are used [17]. When a source is located at (x', y', z') in region 1 as shown in Figure 3(a) and the virtual conductors lay on the $x = 0$ plane, an image source at $(-x', y', z')$ is created by the image theory and the direction of image source is reversed only in the case of PMC. If the original and image sources considered by virtual PEC and PMC are individually added or subtracted, the original or image source with double amplitude only remains, respectively. This principle can be articulated to the reflection and transmission coefficients for the Green's functions in each region because the fields in region 1 are related to the reflection with the original source and the transmission to region 3 is identical to the reflection to region 3 by means of the image source. In other words, with the sum and difference of the reflection coefficients derived from the existence of virtual PEC or PMC, the reflection and transmission coefficients in regions 1 and 3 are represented simply, respectively.

For scattering waves in each region of slab, the Sommerfeld identity of the Green's function being available to solve 2-dimensional problem is applied [20] and expanded with TM_x mode as the electric source of x-direction [19]. Since the coordinate system divided into vertical and horizontal directions to the slab is convenient, the coordinate system of x, γ, and ψ is employed in this analysis. The relation of the variations of this coordinate system and rectangular coordinate system is as follows: $x = x$, $\gamma = \sqrt{y^2 + z^2}$, and $\psi = \tan^{-1}(y/z)$. When a VED with current moment Il is located at (x', γ', ψ') in region 1, scattering electric field formulations at observation point (x, γ, ψ) in regions 1, 2, and 3 are derived as written in (11), (12), (13), (14), and (15), (16), respectively. The y and z components of the fields are acquired from multiplying the γ components in (12), (14),

and (16) by $\sin(\psi-\psi')$ and $\cos(\psi-\psi')$, respectively.

$$E_x^{S(11)\_P} = \frac{-Il}{4\pi\omega\varepsilon_1}\int_0^\infty \frac{k_\gamma^3}{k_{x1}}\Gamma\left(k_\gamma\right) J_0\left(k_\gamma\left|\gamma-\gamma'\right|\right) e^{jk_{x1}(2a-x-x')}dk_\gamma \quad (11)$$

$$E_\gamma^{S(11)\_P} = \frac{-jIl}{4\pi\omega\varepsilon_1}\int_0^\infty k_\gamma^2\Gamma\left(k_\gamma\right) J_1\left(k_\gamma\left|\gamma-\gamma'\right|\right) e^{jk_{x1}(2a-x-x')}dk_\gamma \quad (12)$$

$$E_x^{S(21)\_P} = \frac{-Il}{4\pi\omega\varepsilon_2}\int_0^\infty \frac{k_\gamma^3}{k_{x1}}T_x^{(21)}(x,k_\gamma)J_0\left(k_\gamma\left|\gamma-\gamma'\right|\right) e^{jk_{x1}(a-x')}dk_\gamma \quad (13)$$

$$E_\gamma^{S(21)\_P} = \frac{Il}{4\pi\omega\varepsilon_2}\int_0^\infty k_\gamma^2 T_\gamma^{(21)}(x,k_\gamma)J_1\left(k_\gamma\left|\gamma-\gamma'\right|\right) e^{jk_{x1}(a-x')}dk_\gamma \quad (14)$$

$$E_x^{S(31)\_P} = \frac{-Il}{4\pi\omega\varepsilon_1}\int_0^\infty \frac{k_\gamma^3}{k_{x1}}T^{(31)}(k_\gamma)J_0\left(k_\gamma\left|\gamma-\gamma'\right|\right) e^{jk_{x1}(2a+x-x')}dk_\gamma \quad (15)$$

$$E_\gamma^{S(31)\_P} = \frac{jIl}{4\pi\omega\varepsilon_1}\int_0^\infty k_\gamma^2 T^{(31)}(k_\gamma)J_1\left(k_\gamma\left|\gamma-\gamma'\right|\right) e^{jk_{x1}(2a+x-x')}dk_\gamma \quad (16)$$

where

$$\Gamma\left(k_\gamma\right) = \left\{\Gamma_e\left(k_\gamma\right)+\Gamma_m\left(k_\gamma\right)\right\}/2 \quad (17)$$

$$T_x^{(21)}\left(x,k_\gamma\right) = \left\{T_e\left(x,k_\gamma\right)+T_m\left(x,k_\gamma\right)\right\}/2 \quad (18)$$

$$T_\gamma^{(21)}\left(x,k_\gamma\right) = \frac{k_{x2}}{2k_{x1}}\left\{T_m(x,k_\gamma)\cot\left(k_{x2}x\right)-T_e\left(x,k_\gamma\right)\tan\left(k_{x2}x\right)\right\} \quad (19)$$

$$T^{(31)}\left(k_\gamma\right) = \left\{\Gamma_e\left(k_\gamma\right)-\Gamma_m\left(k_\gamma\right)\right\}/2 \quad (20)$$

$$k_{x1} = \begin{cases} \sqrt{k_1^2-k_\gamma^2}, & k_1 < k_\gamma \\ -\sqrt{k_1^2-k_\gamma^2}, & k_1 > k_\gamma \end{cases} \quad (21)$$

$$k_{x2} = \begin{cases} \sqrt{k_2^2-k_\gamma^2}, & k_1 < k_\gamma \\ -\sqrt{k_2^2-k_\gamma^2}, & k_1 > k_\gamma \end{cases} \quad (22)$$

$\varepsilon_1 = \varepsilon_0$, $\varepsilon_2 = \varepsilon_r\varepsilon_0 - j\sigma/\omega$, and $J_n(x)$ is the Bessel function of the first kind of order n. The reflection and two transmission coefficients corresponding to each region are described in (17)–(20). As denoted in (18) and (19), the x and γ components of the fields in region 2 have the different forms of transmission coefficient because the coefficient comprises the x coordinate of observation point and the second-order and first-order partial differentials with respect to the x variable are involved, respectively. The reflection and transmission coefficients Γ_e, T_e and Γ_m, T_m calculated by the placement of virtual PEC and PMC, respectively, are explained in the Appendix B. k_{x1} and k_{x2} are the wavenumbers of x-direction in regions 1 and 2, respectively, and k_γ is

the wavenumber of γ-direction irrelevant to regions. In order to satisfy the radiation condition, the k_{x1} and k_{x2} are negative when k_γ is smaller than k_1.

The separation of CWs, CLWs, and CGWs debated in Section 2 signifies the extraction of the waves contributed independently from only the wavenumber of longitudinal direction. Hence, in the analysis for slab, the results served by only the wavenumber $k_z = k_\gamma \cos\alpha$ in $\mathbf{k}_\gamma$ illustrated in Figure 3(b) are required. With the reference to Figure 3(b), the propagation of γ-direction is expressed as $\mathbf{k}_\gamma \cdot |\gamma - \gamma'| = k_\gamma |\gamma - \gamma'| \cos(\alpha - (\psi - \psi'))$, and the condition, in which the inner product becomes the function of only k_z, is $\psi - \psi' = 0$ or π. Namely, when a source and an observation point are placed in same xz-plane, the purpose of this paper is accomplished.

4. NUMERICAL RESULTS AND DISCUSSIONS

4.1. Field Distributions in Longitudinal Section

In this section, firstly, in order to verify the reliabilities of the scattering electric field formulations constructed in Section 3, the comparison of the results calculated by the FDTD method and with the analytical solutions is performed. With the approximate estimation from the average circumference of a Japanese forearm [23], the parameter a, which indicates the radius of cylinder and half the thickness of slab, is set as 0.050 m for the human arm. The operating frequency is 2.45 GHz, and the inner cylinder and inner slab assumed to be a homogeneous single tissue have electrical properties of the 2/3-muscle equivalent tissue, $\sigma = 1.16$ S/m, $\varepsilon_r = 35.15$ at 2.45 GHz [24]. The source, which is a linear VED of 0.030 m length, is located at 0.010 m away from the cylinder or slab surface. With the coordinate systems in Figures 2(a) and 3(a), the coordinates of feeding point placed at the center of source are $(\rho', \phi', z') = (x', y', z') = (0.050\,\mathrm{m}, 0, 0)$. The observation plane is xz-plane at $y = 0$.

In the calculations with the FDTD method, the cell size is $\Delta x = \Delta y = \Delta z = 0.002$ m and the perfect matching layer (PML) of eight layers is used as the absorbing boundary condition. The cylinder is extended into inner PML for materialization of the infinity of z-direction and the slab is at yz-plane. In the radiation problems with analytical solutions, the incident electric fields $\mathbf{E}^0$ in (1) and (3) are easily achieved by the analysis of TM_x mode with the free-space Green's function of scalar wave equation [19]. For the scattering electric fields, the integrals over the wavenumbers k_z and k_γ in Sections 3.1 and 3.2 are worked out by applying the Gauss-Legendre integration excluding the branch-point singularities at $k_z = \pm k_1$

and $k_\gamma = k_1$, respectively. The numerical method for the integrals is demonstrated concretely in the Appendix C. The total electric field distributions estimated with cylinder- and slab-body models are exhibited in Figures 4 and 5, respectively. Each (a) and (b) in Figures 4 and 5 are the results calculated by the FDTD method and with the analytical solutions, respectively.

The FDTD method was programmed with FORTAN, but the calculations with analytical solutions received assistance from MATLAB function library in order to secure reliable values of the Bessel and Hankel functions. Since the FDTD method which outputs

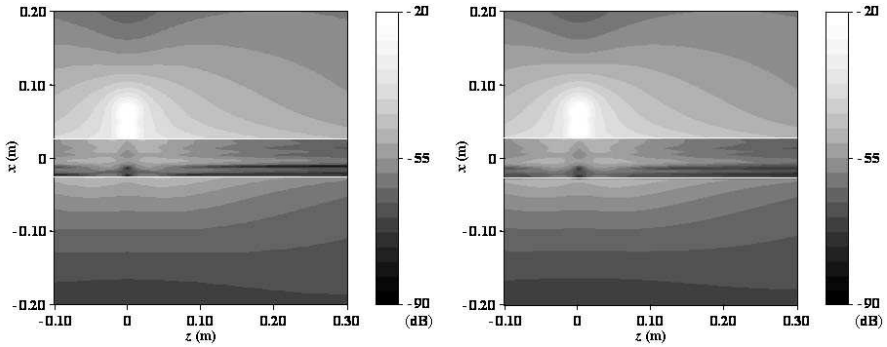

Figure 4. Total electric field distributions estimated with cylinder-body model. (a) By FDTD method. (b) With analytical solutions.

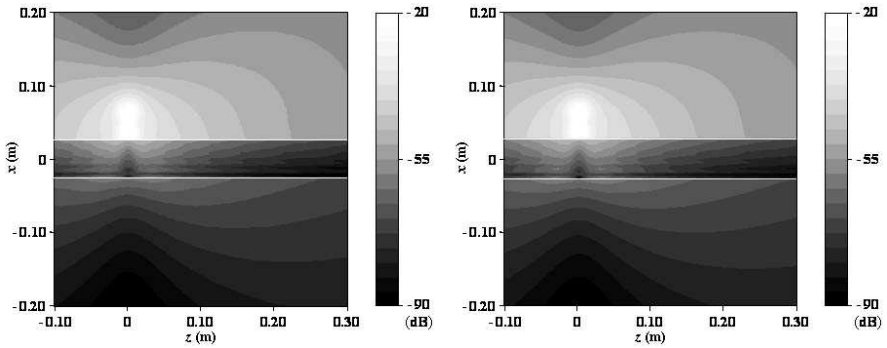

Figure 5. Total electric field distributions estimated with slab-body model. (a) By FDTD method. (b) With analytical solutions.

only total electric fields is progressed with the differential forms of the Maxwell's equations, the computation is completed in the relatively short calculation time regardless of body-model type but demands a high memory, that is 413 Mbytes for Figures 4(a) and 5(a), owing to saving all computation data with respect to time in a restricted calculation domain. On the other hand, the analytical solutions which acquire separately scattering electric fields consist of integral expression; therefore the calculation needs a considerable time for precise results involved with strict convergence conditions of the integrals, but the computational memory-cost is very low because the saving spaces are requisite only for a temporary value in repetition processing for convergence at an observation point and final data at all calculation region. In order to obtain Figures 4(b) and 5(b), 42 Mbytes memory was used. The analytical solutions for cylinder-body model require a quite high computational time-cost due to the consideration for convergences of both integral variable k_z and summation variable n.

In Figures 4 and 5, the levels of each point are displayed as relative values normalized by the absolute value of total electric field at $(x, y, z) = (0.050\,\mathrm{m}, 0, 0.002\,\mathrm{m})$. The white lines in the results indicate the interfaces between the human body and the free space. In Figure 4 of cylinder-body model, the results by the FDTD method and with the eigenfunction solutions are in near-perfect agreement except that a very slight difference is observed at the opposite region of source. That is an error in the FDTD method which cannot take shape the calculation model of an ideal circular transversesection. In the case of the slab-body model, Figure 5 shows that the results, calculated by the FDTD method and with the analytical solutions, are in perfect agreement.

As the second subject in this section, the specific cylinder waves generated only in cylinder structure are extracted and the general characteristics about the components of scattering waves mentioned in Section 2 are discussed. Figures 6(a) and (b) exhibit the scattering electric fields analyzed with circular-cylinder and planar-slab structures, respectively. These are that the incident waves in the total fields shown in Figures 4(b) and 5(b), respectively, are removed. Through the subtraction of the result viewed in Figure 6(b) from the result displayed in Figure 6(a), Figure 6(c) shows the field distribution of CWs and CLWs extracted outside the cylinder and CGWs inside.

In Figure 6(b), the scattering fields inner slab are distributed with not a constantly decreasing form but partially folding shapes. This describes the GW mode constituted by multiple reflections inner slab, but the mode cannot be discerned distinctly by the large attenuation

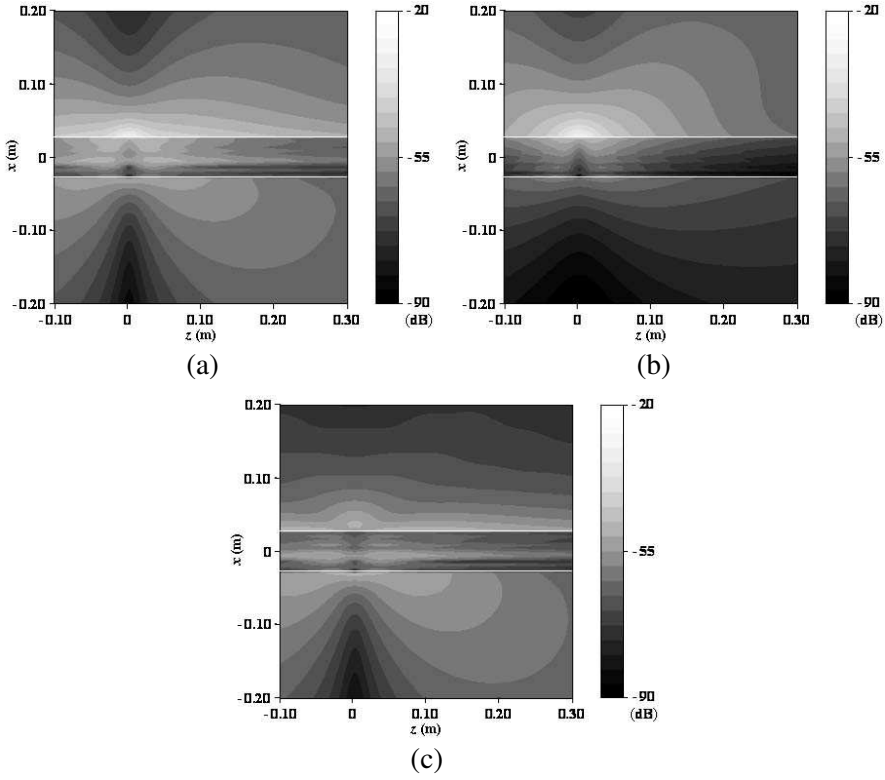

Figure 6. Scattering electric field distributions. (a) With circular-body model. (b) With slab-body model. (c) Extracted CWs, CLWs, and CGWs.

in z-direction as well as x-direction due to the high conductivity. Little contribution of the SW and LW modes in region 1 and the LW mode in region 3 can be inferred with such lossy characteristic. In actuality, the irregular levels such as a ripple related to natures of the SW and LW modes are not detected in the vicinity of the interfaces. Therefore, the RW mode in region 1 and the TW mode in region 3 are dominant in scattering wave modes. The fields near the slab in region 1 are distributed like the propagation along the interface such as the SW mode, but it is associated with incident and reflected angles of waves in the RW mode. When a source approaches the slab, the phenomenon of such field distribution is shown noticeably. The unique radiation characteristics of VED are transformed by RWs but it is kept basically except for the distribution near the slab. Since the TW mode in region 3 has direct propagation paths penetrating region 2 and the amount

of attenuation in region 2 is determined by lengths of such paths, the spread flat field distribution compared to the radiation pattern of general VED is displayed in region 3.

In Figure 6(a), the levels of the fields in regions 1 and 3 are little different generally because the regions are connected spatially in essence. In results related to cylinder structure, the region 3, which is designated for convenience in Section 4, means actually the opposite side of the cylinder as the region 1 identified in Section 3.1. In Figure 6(c), the CGWs in region 2 are concentrated on a specific z-axis and it is preserved in Figure 6(a). In case of the SAR evaluation in the human body, this result is contrasted with the general view, which the SAR is decreased gradually when an evaluation point is moved on the inward side of the human body. This manifests that propagation characteristics based on geometrical structure of a subject should be considered for wave-examinations inner human body such as the SAR evaluation. In Figure 6(c), the dissimilarity between the field distributions in regions 1 and 3 shows the offset and complement between CWs and CLWs. Although the CW mode is influenced by the conductivity inner cylinder, the intensities of CWs in regions 1 and 3 are almost continuous because the CW mode is the propagation along the azimuthal surface of cylinder. On the other hand, CLWs in regions 1 and 3 are discontinuous and the reason can be explained by the operation of the CLW mode. The CLWs are created when CGWs with azimuthal multi-reflection are leaked to the outside of the cylinder. The propagation-path lengths of the CGWs arrived at the interface between regions 1 and 2 are relatively longer than the path lengths to the interface between regions 2 and 3. As the amount of loss and the phase variation inner cylinder are connected to the path lengths, the CLWs in regions 1 and 3 have great differences. Such characteristics of CWs and CLWs cause the different field distributions in regions 1 and 3.

4.2. Scattering Waves with Variations of Cylinder Radius and Operating Frequency

In analysis with cylinder-body model for BANs, the considerable parameters, which have influence on overall results, are cylinder radius and operating frequency. The variation of cylinder radius affects sensitively scattering waves, especially CWs, CLWs, and CGWs, and the relative researches have been investigated quite a while ago. Due to the fact that electrical properties of the human body vary with frequency [24], the operating frequency becomes a very important consideration for BANs.

With the variations of parameter a and operating frequency,

Figures 7 and 8 show absolute values of scattering electric fields. In Figures 7 and 8, each (a) displays the results evaluated with cylinder-body model, and each (b) is the outcomes with slab-body model, and each (c) exhibits the intensities of CWs and CLWs separated by taking each (b) from each (a). The parameter a means half of slab thickness or cylinder radius, and it has the range covered comprehensively from the human arm to the human torso [23]. A source employed in Section 4.2 is the infinitesimal VED located at $(x', y', z') = (a + 0.001\,\mathrm{m}, 0, 0)$ with the current moment of $0.02\,\mathrm{A{\cdot}m}$. The source coordinates at the closest point to the cylinder surface is chosen because the largest levels of scattering waves are anticipated. The observation points in Figures 7 and 8, respectively, are $(x, y, z) = (a+0.001\,\mathrm{m}, 0, 0)$ in region

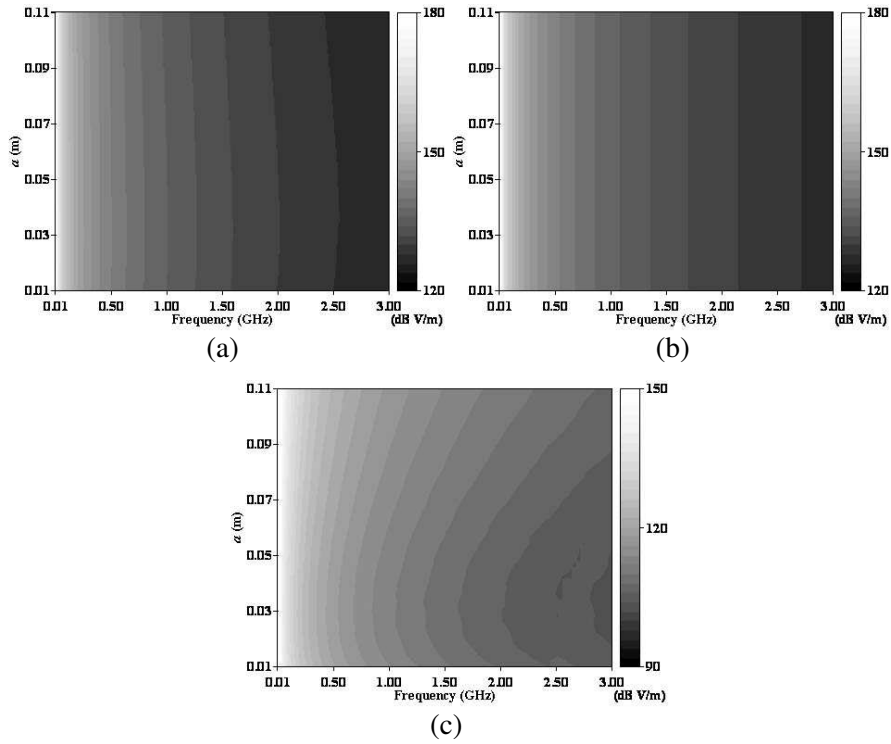

Figure 7. Scattering electric field intensities with variations of parameter a and operating frequency when source is located at $(x', y', z') = (a + 0.001\,\mathrm{m}, 0, 0)$ and observation is at $(x, y, z) = (a + 0.001\,\mathrm{m}, 0, 0)$. (a) With circular-body model. (b) With slab-body model. (c) Extracted CWs, CLWs, and CGWs.

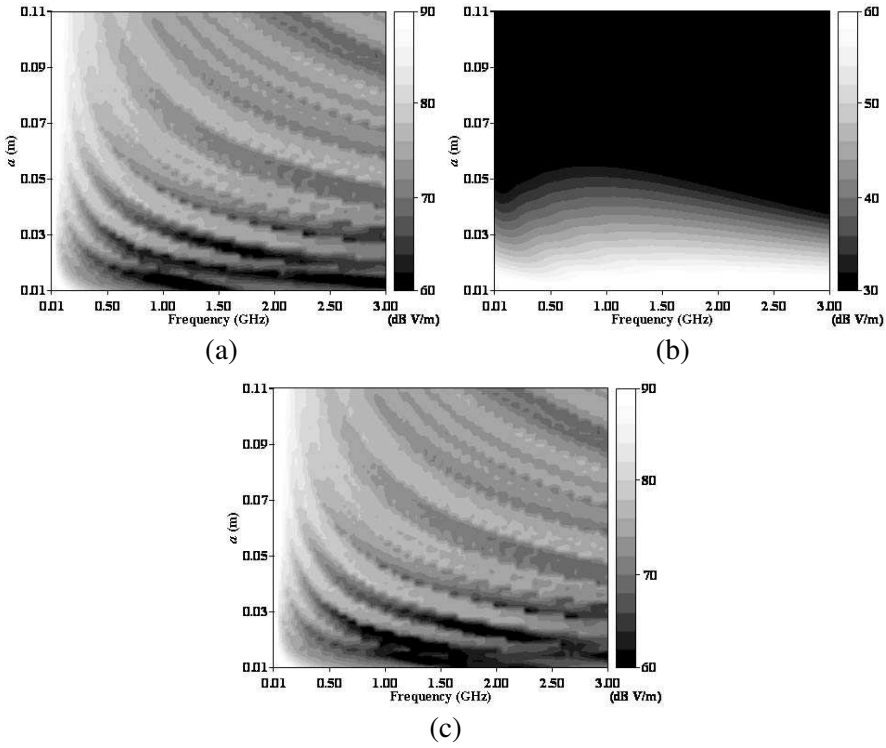

Figure 8. Scattering electric field intensities with variations of parameter a and operating frequency when source is located at $(x', y', z') = (a + 0.001\,\text{m}, 0, 0)$ and observation is at $(x, y, z) = (-a - 0.001\,\text{m}, 0, 0)$. (a) With circular-body model. (b) With slab-body model. (c) Extracted CWs, CLWs, and CGWs.

1 and $(-a - 0.001\,\text{m}, 0, 0)$ in region 3 in order to investigate scattering characteristics excluded the propagation toward z-direction. In the calculations, electrical features of the 2/3-muscle equivalent tissue in accordance with operating frequency were used [24]. Since it is hard to determine the standard value for normalization when the frequency sweep is examined, all values of results in this section are expressed with dB V/m, which the absolute electric field unit V/m is converted on a logarithmic scale in decibels.

As the scattering waves at same observation point with source coordinates, in Figures 7(a) and (b), remarkable points are that the results with cylinder and slab structures are little different and are largely unchanged with the variation of parameter a. These

results demonstrate that the most influential scattering component in electrical characteristics of the source is the RWs when a source is adjacent to the surface of structure analyzed. This conclusion can also be confirmed by the relatively very low intensities of CWs and CLWs shown in Figure 7(c). The contributions of SWs and LWs may be negligible in a similar context discussed in Section 4.1. In the design of a wearable device for BANs, it cannot avoid the change of device characteristics, such as the input impedance or current distribution, owing to scattering waves by the human body. Thus the analytical evaluation of the scattering waves is required for the effectual design of device. Figure 7 attests that results with slab-body model are available for the analytical calculation with such purpose, and the use of slab-body model may be more useful because the convergence speed is very slow in the numerical computation with cylinder-body model.

Figures 8(a) and (b) are the results of scattering waves at the closest observation point to the surface of each structure in region 3, and Figure 8(c) shows the intensities of CWs and CLWs. Contrary to the results at the observation point in region 1, it can be judged that the specific waves generated by the cylindrical geometry are dominant in region 3. The TWs and LWs shown in Figure 8(b) contribute to the overall scattering waves only when the cylinder radius is less than 0.022 m. From Figure 8(b), it is reconfirmed that propagationpath lengths of the TW and LW modes are increased due to the increase of cylinder radius and the levels of TWs and LWs are decreased. The attenuation by the conductivity proportional to operating frequency also is perceived. In Figure 8(c), the sections of levels decreased by the counterbalance between CWs and CLWs are observed periodically in connection with the cylinder-radius axis.

The CW and CLW modes propagate toward the longitudinal direction simultaneously with the azimuthal direction. For examination of wave propagation along the longitudinal direction, the scattering waves estimated with slab-body model and extracted CWs and CLWs at 2.45 GHz are shown in Figure 9 when the observation points are set as $(x, y, z) = (a + 0.001\,\mathrm{m}, 0, z)$ in region 1 and $(-a - 0.001\,\mathrm{m}, 0, z)$ in region 3. The parameter a is set up as 0.025 m and 0.075 m represented as the human arm and thigh, respectively [23]. These results display the components of scattering waves generated by the cylinder-body model at a look. In Figure 9(a), the CWs and CLWs in regions 1 are almost identical with the waves in region 3. In Figure 9(b), the offsetting between CWs and CLWs in region 1 is observed but the waves in region 3 are similar to the waves shown in Figure 9(a). In the results of these CWs and CLWs, it is noticeable that the peak levels of the fluctuations of the waves in region 3 are

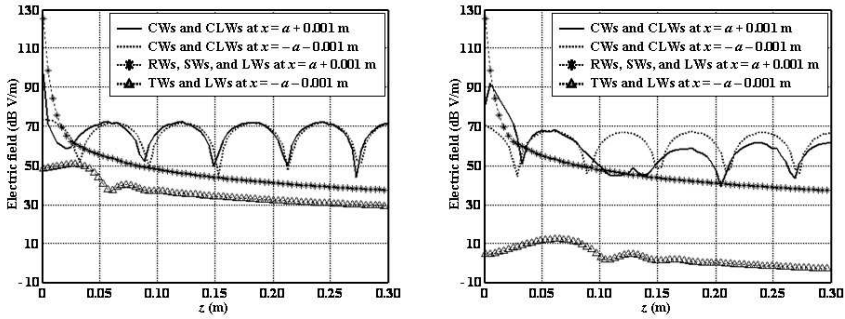

Figure 9. Components of scattering waves in cylinder-body model with variation of observation point along z-axis. (a) At 2.45 GHz and $a = 0.025$ m. (b) At 2.45 GHz and $a = 0.075$ m.

maintained almost in spite of the propagation along z-axis. With the reference to the operation of CLW mode and the almost continuity of CWs in regions 1 and 3 discussed in Section 4.1, the existence of CWs with low attenuation dominated in the vicinity of the cylinder surface can be demonstrated In Figures 9(a) and (b), the graphs of RWs, SWs, and LWs with the exponential decreasing are perfectly identical. These can be regarded as the extension of results shown in Figure 7(b). The levels of RWs, SWs, and LWs only near the source are higher than the intensities of CWs and CLWs. It is confirmed that the TW and LW modes are insignificant for scattering waves in region 3 regardless of the movement of observation point along z-axis. As the conclusion obtained from Figure 9, when a source is located near the cylinder surface, it can say that the dominant propagation mode toward the cylinder axis in the vicinity of the cylinder surface is the CW mode except for the area near a source.

5. CONCLUSIONS

In this paper, in order to investigate separately the components of scattering waves generated in cylinder-body model for BANs, the scattering wave modes in circular-cylinder and planar-slab structures were analyzed, and the method of quantitative computation of specific waves, which are CWs, CLWs, and CGWs, generated only in cylindrical geometry was suggested. Additionally, the scattering electric field formulations for the cylinder- and slab-body models, respectively, were derived from the eigenfunction solutions and by using

the virtual PEC and PMC. The exactitudes of the formulations were verified by the comparisons with the total field distributions calculated by the FDTD method.

With a finite linear VED and the 2/3-muscle equivalent tissue as the human body, the scattering waves in cylinder- and slab-body models were calculated on the common plane of two models, and CWs, CLWs, and CGWs were extracted by the difference of the scattering waves. Each scattering mode in optically illuminated area, inner body, and in non-illuminated zone was estimated and analyzed based on the results.

The estimations with the variations of operating frequency and cylinder radius were accomplished. From the results, when a source is adjacent to cylinder surface, it was confirmed that the most influential scattering component in electrical characteristics of the source was RWs, and the CWs and CLWs modes were the dominant modes at the opposite side of the cylinder with the cylinder radius larger than 0.022 m. Furthermore, the electric field intensities with the variation of observation point along the longitudinal direction were calculated and the existence of CWs with low attenuation dominated in the vicinity of the cylinder surface was demonstrated.

In the future, for more intensive examination of scattering waves, the analytical solutions will be expanded to multi-layered models of the human body.

APPENDIX A. SCATTERING COEFFICIENTS FOR CIRCULAR-CYLINDER STRUCTURE

For construction of scattering field formulations associated with an infinite cylinder, it is necessary firstly to expand the eigenfunction of the Green's function in the free space. In accordance with the kind of cylinder, scattering coefficients are attached to the expanded eigenfunction solutions. By the method to satisfy boundary conditions at the interface $\rho = a$, between the cylinder and the external environment, the coefficients are determined with the forms of simultaneous equations. In the case of a lossy-dielectric cylinder conducted in this paper, the scattering coefficients are arranged as follows:

$$A_1 = -\frac{J_n(k_{\rho 1}a)}{H_n^{(2)}(k_{\rho 1}a)} - \frac{j2}{\pi(k_{\rho 1}a)} \frac{T_n(k_{\rho 1}, k_{\rho 2}; a)}{\left[(k_{\rho 1}a) H_n^{(2)}(k_{\rho 1}a)\right]^2 U_n(k_{\rho 1}, k_{\rho 2}; a)} \quad \text{(A1)}$$

$$B_1 = \frac{2}{\pi(k_{\rho 1}a)} \frac{W(k_{\rho 1}, k_{\rho 2}; a)}{a\left[(k_{\rho 1}a) H_n^{(2)}(k_{\rho 1}a)\right]^2 U_n(k_{\rho 1}, k_{\rho 2}; a)} \left(\frac{nk_z}{k_1}\right) \quad \text{(A2)}$$

$$C_1 = -\frac{J_n(k_{\rho 1}a)}{H_n^{(2)}(k_{\rho 1}a)} - \frac{j2}{\pi(k_{\rho 1}a)} \frac{S_n(k_{\rho 1}, k_{\rho 2}; a)}{\left[(k_{\rho 1}a) H_n^{(2)}(k_{\rho 1}a)\right]^2 U_n(k_{\rho 1}, k_{\rho 2}; a)} \quad \text{(A3)}$$

$$D_1 = B_1 \quad \text{(A4)}$$

$$a_2 = -\frac{j2}{\pi(k_{\rho 1}a)} \frac{\mu T_n(k_{\rho 1}, k_{\rho 2}; a)}{(k_{\rho 2}a)^2 J_n(k_{\rho 2}a) H_n^{(2)}(k_{\rho 2}a) U_n(k_{\rho 1}, k_{\rho 2}; a)} \quad \text{(A5)}$$

$$b_2 = \frac{2}{\pi(k_{\rho 1}a)} \frac{\sqrt{\mu\varepsilon} W(k_{\rho 1}, k_{\rho 2}; a)}{a(k_{\rho 2}a)^2 J_n(k_{\rho 2}a) H_n^{(2)}(k_{\rho 2}a) U_n(k_{\rho 1}, k_{\rho 2}; a)} \left(\frac{nk_z}{k_1}\right) \quad \text{(A6)}$$

$$c_2 = -\frac{j2}{\pi(k_{\rho 1}a)} \frac{\sqrt{\mu\varepsilon}\, S_n(k_{\rho 1}, k_{\rho 2}; a)}{(k_{\rho 2}a)^2 J_n(k_{\rho 2}a) H_n^{(2)}(k_{\rho 2}a) U_n(k_{\rho 1}, k_{\rho 2}; a)} \quad \text{(A7)}$$

$$d_2 = \sqrt{\varepsilon/\mu} b_2 \quad \text{(A8)}$$

$$U_n(k_{\rho 1}, k_{\rho 2}; a) = S_n(k_{\rho 1}, k_{\rho 2}; a) T_n(k_{\rho 1}, k_{\rho 2}; a) - \left(\frac{nk_z}{k_1 a}\right)^2 (W(k_{\rho 1}, k_{\rho 2}; a))^2 \quad \text{(A9)}$$

$$S_n(k_{\rho 1}, k_{\rho 2}; a) = \frac{\partial H_n^{(2)}(k_{\rho 1}a)\Big/\partial a}{(k_{\rho 1}a)^2 H_n^{(2)}(k_{\rho 1}a)} - \mu \frac{\partial J_n(k_{\rho 2}a)/\partial a}{(k_{\rho 2}a)^2 J_n(k_{\rho 2}a)} \quad \text{(A10)}$$

$$T_n(k_{\rho 1}, k_{\rho 2}; a) = \frac{\partial H_n^{(2)}(k_{\rho 1}a)\Big/\partial a}{(k_{\rho 1}a)^2 H_n^{(2)}(k_{\rho 1}a)} - \varepsilon \frac{\partial J_n(k_{\rho 2}a)/\partial a}{(k_{\rho 2}a)^2 J_n(k_{\rho 2}a)} \quad \text{(A11)}$$

$$W(k_{\rho 1}, k_{\rho 2}; a) = \frac{1}{(k_{\rho 1}a)^2} - \frac{1}{(k_{\rho 2}a)^2} \quad \text{(A12)}$$

where $\varepsilon = (\varepsilon_r\varepsilon_0 - j\sigma/\omega)/\varepsilon_0$ and $\mu = \mu_0/\mu_0 = 1$ are the ratios of permittivity and permeability, respectively, between regions 1 and 2 in Figure 2.

APPENDIX B. REFLECTION AND TRANSMISSION COEFFICIENTS FOR PLANAR-SLAB STRUCTURE

When the PEC or PMC is on $x = 0$ plane in Figure 3(a), the reflection and transmission coefficients can be solved easily by the transmission-line theory with respect to the x-direction. The input impedances for each case at the interface $x = a$ between regions 1 and 2 are firstly yielded with the transmission-line length a and the wave impedance $k_{x2}/(\omega\varepsilon_2)$ of TM mode in region 2. Then, from the wave impedances $k_{x1}/(\omega\varepsilon_1)$ in region 1 and the input impedances, the reflection coefficients of PEC and PMC cases are derived as written in (B1)

and (B2), respectively. The transmission coefficients for the fields inner slab maintain the general relation between the Fresnel transmission and reflection coefficients, but the boundary conditions at $x = 0$ and the continuity at $x = a$ should be applied additionally [22]. Those are to append the terms of $\cos(k_{x2}x)/\cos(k_{x2}a)$ and $\sin(k_{x2}x)/\sin(k_{x2}a)$ in the cases of PEC and PMC, respectively. The transmission coefficients of each case are arranged in (B3) and (B4), respectively.

$$\Gamma_e(k_\gamma) = -\frac{jk_{x2}\tan(k_{x2}a) - \varepsilon k_{x1}}{jk_{x2}\tan(k_{x2}a) + \varepsilon k_{x1}} \tag{B1}$$

$$\Gamma_m(k_\gamma) = -\frac{jk_{x2}\cot(k_{x2}a) + \varepsilon k_{x1}}{jk_{x2}\cot(k_{x2}a) - \varepsilon k_{x1}} \tag{B2}$$

$$T_e(x, k_\gamma) = \frac{j2\varepsilon\ k_{x1}\cos(k_{x2}x)}{jk_{x2}\sin(k_{x2}a) + \varepsilon k_{x1}\cos(k_{x2}a)} \tag{B3}$$

$$T_m(x, k_\gamma) = \frac{-j2\varepsilon\ k_{x1}\sin(k_{x2}x)}{jk_{x2}\cos(k_{x2}a) - \varepsilon k_{x1}\sin(k_{x2}a)} \tag{B4}$$

where $\varepsilon = \varepsilon_2/\varepsilon_1 = (\varepsilon_r\varepsilon_0 - j\sigma/\omega)/\varepsilon_0$.

APPENDIX C. NUMERICAL METHOD FOR ANALYTICAL SOLUTIONS

The integrals in Section 3.1 are estimated with the integration path drawn in Figure C1. Because the integrands have branch-point singularities at $k_z = \pm k_1$, the integration path takes a detour round at the points. The analysis associated with the branch points is accomplished with asymptotic techniques [20]. However, in this

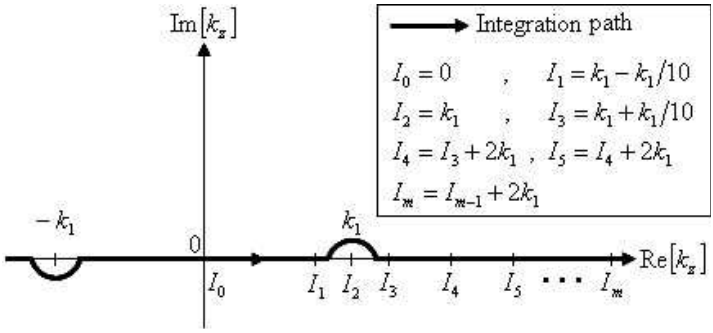

Figure C1. In circular-cylinder structure, integration path in complex k_z plane and sub-integral interval points for numerical computation in $\mathrm{Re}[k_z] \geq 0$.

paper to pursue an exact numerical analysis, the evaluations at branch points are excluded purposefully by using the Gauss-Legendre integration which is extreme accurate without the end points of integral interval [25].

As described in (C1), the interval of the integrals in Section 3.1 can be separated into $k_z \leq 0$ and $k_z \geq 0$. As derived in (C2), the integral for $k_z \geq 0$ can be expressed as the summation of sub-integrals with closed intervals $[I_{m-1}, I_m]$ shown in Figure C1, and each sub-integral can be converted by the Gauss-Legendre integration formulation. The end points of closed intervals are duplicated owing to the continuity of intervals, but actual calculation has no regard for such duplications because the end points are ruled out as sampling points determined by the Gauss-Legendre integration method.

$$\mathbf{E}^{S\_C}(k_z, n) = \int_{-\infty}^{\infty} dk_z \sum_{n=0}^{\infty} \mathbf{f}(k_z, n)$$

$$= \int_{-\infty}^{0} dk_z \sum_{n=0}^{\infty} \mathbf{f}(k_z, n) + \int_{0}^{\infty} dk_z \sum_{n=0}^{\infty} \mathbf{f}(k_z, n) \tag{C1}$$

$$\int_0^{\infty} dk_z \sum_{n=0}^{\infty} \mathbf{f}(k_z, n) = \sum_{n=0}^{\infty} \int_0^{\infty} \mathbf{f}(k_z, n)\, dk_z$$

$$= \sum_{n=0}^{\infty} \sum_{m=1}^{\infty} \int_{I_{m-1}}^{I_m} \mathbf{f}_m(k_z(m), n)\, dk_z$$

$$= \sum_{n=0}^{\infty} \sum_{m=1}^{\infty} \left[\frac{I_m - I_{m-1}}{2} \sum_{i=0}^{h} w(i)\, \mathbf{f}_m(k_z(m,i), n) \right]$$

$$= \sum_{m=1}^{\infty} \left[\frac{I_m - I_{m-1}}{2} \sum_{i=0}^{h} w(i) \left\{ \sum_{n=0}^{\infty} \mathbf{f}_m(k_z(m,i), n) \right\} \right] = \sum_{m=1}^{\infty} \mathbf{g}_m \tag{C2}$$

where

$$k_z(m,i) = \frac{I_m + I_{m-1}}{2} + \frac{I_m - I_{m-1}}{2} \alpha(i) \tag{C3}$$

$$w(i) = \frac{1}{\partial P_{h+1}(\alpha(i))/\partial \alpha(i)} \int_{-1}^{1} \frac{P_{h+1}(\alpha)}{\alpha - \alpha(i)} d\alpha \tag{C4}$$

$P_{h+1}(\alpha)$ is the Legendre polynomial of $(h+1)$ degrees and $\alpha(i)$ is the root of $P_{h+1}(\alpha) = 0$. The weighting coefficient in the Gauss-Legendre integration is symbolized as $w(i)$.

The sub-integral intervals and the degree of the Legendre polynomial are decisive factors for the accuracy of original integral. In

relation to the sub-integral intervals, because the branch point $k_z = k_1$ is the discontinuity point of original integral, above all, the interval should divide into $[0, k_1]$ and $[k_1, \infty)$. And then, as the points I_1 and I_3 shown in Figure C1, it is necessary that the intervals are appropriately subdivided with a same distance away from the branch point since the value of integrand near the branch point is rapidly varied. The interval beyond point I_3 is sectioned with a proper gap for the convergence discernment of integration-path length. The Legendre polynomial of 41 degrees ($h = 40$) was utilized for the results in this paper, and this means that sub-integrals are estimated by the 41 sampling points inside the interval $[I_{m-1}, I_m]$. The integral for $k_z \leq 0$ has to be expanded with symmetrical sub-integral intervals with respect to $k_z = 0$.

The individual convergences with respect to n and m in (C2) are the prerequisites for results with finite values. As discriminants for the convergences, respectively, (C5) and (C6) are employed.

$$\left|\frac{\mathrm{Re}\left[\sum_{n=0}^{t}\mathbf{f}_m\right]-\mathrm{Re}\left[\sum_{n=0}^{t-1}\mathbf{f}_m\right]}{\mathrm{Re}\left[\sum_{n=0}^{t}\mathbf{f}_m\right]}\right|\leq C_n \text{ and } \left|\frac{\mathrm{Im}\left[\sum_{n=0}^{t}\mathbf{f}_m\right]-\mathrm{Im}\left[\sum_{n=0}^{t-1}\mathbf{f}_m\right]}{\mathrm{Im}\left[\sum_{n=0}^{t}\mathbf{f}_m\right]}\right|\leq C_n \quad \text{(C5)}$$

$$\left|\frac{\mathrm{Re}\left[\sum_{m=1}^{s}\mathbf{g}_m\right]-\mathrm{Re}\left[\sum_{m=1}^{s-1}\mathbf{g}_m\right]}{\mathrm{Re}\left[\sum_{m=1}^{s}\mathbf{g}_m\right]}\right|\leq C_m \text{ and } \left|\frac{\mathrm{Im}\left[\sum_{m=1}^{s}\mathbf{g}_m\right]-\mathrm{Im}\left[\sum_{m=1}^{s-1}\mathbf{g}_m\right]}{\mathrm{Im}\left[\sum_{m=1}^{s}\mathbf{g}_m\right]}\right|\leq C_m \quad \text{(C6)}$$

The results in this paper were computed with convergence conditions C_n and C_m of 0.0001 and 0.0010, respectively. In relation to the choice of the convergence conditions, those C_n and C_m have the difference of scattering field intensities within 0.0010% near the interface between the cylinder and the free space.

In the evaluation for planar-slab structure, k_z in (C1) and (C2) is corresponded to k_γ with interval $[0, \infty)$. All terms with respect to n are removed and the discriminant of (C6) is involved only. The convergence condition $C_m = 0.0010$ was used for the analysis with slab-body model.

REFERENCES

1. Weiser, M., "The computer for the twenty-first century," *Scientific American*, 66–75, Sep. 1991.
2. Zimmerman, T. G., "Personal area networks: Near-field intra-

body communication," *IBM Systems Journal*, Vol. 35, No. 3, 609–617, 1996.

3. Steinhaus, B. M., R. E. Smith, and P. Crosby, "The role of telecommunications in future implantable device systems," *Proc. IEEE Conference on Medicine and Biology*, 1013–1014, Nov. 1994.
4. Hall, P. S. and Y. Hao, *Antennas and Propagation for Body-centric Wireless Communications*, Artech House Norwood, MA, 2006.
5. Klemm, M. and G. Troester, "Textile UWB antennas for wireless body area networks," *IEEE Trans. Antennas and Propagation*, Vol. 54, No. 11, 3192–3197, Nov. 2004.
6. Haga, N., K. Saito, M. Takahashi, and K. Ito, "Characteristics of cavity slot antenna for body-area networks," *IEEE Trans. Antennas and Propagation*, Vol. 57, No. 4, 837–843, Apr. 2009.
7. Izdebski, P. M., H. Rajagopalan, and Y. Rahmat-Samii, "Conformal ingestible capsule antenna: A novel chandelier meandered design," *IEEE Trans. Antennas and Propagation*, Vol. 57, No. 4, 900–909, Apr. 2009.
8. Hall, P. S., Y. Hao, Y. I. Nechayev, A. Alomainy, C. C. Constantinou, C. Parini, M. R. Kamarudin, T. Z. Salim, D. T. M. Hee, R. Dubrovka, A. S. Owadally, W. Song, A. Serra, P. Nepa, M. Gallo, and M. Bozzetti, "Antennas and propagation for on-body communication systems," *IEEE Antennas and Propagation Mag.*, Vol. 49, No. 3, 41–58, Jun. 2007.
9. Pelosi, M., O. Franek, M. B. Knudsen, M. Christensen, and G. F. Pedersen, "A grip study for talk and data modes in mobile phones," *IEEE Trans. Antennas and Propagation*, Vol. 57, No. 4, 856–865, Apr. 2009.
10. Wang, Q., T. Tayamachi, I. Kimura, and J. Wang, "An on-body channel model for UWB body area communications for various postures," *IEEE Trans. Antennas and Propagation*, Vol. 57, No. 4, 991–998, Apr. 2009.
11. Fujii, K., M. Takahashi, and K. Ito, "Electric field distributions of wearable devices using the human body as a transmission channel," *IEEE Trans. Antennas and Propagation*, Vol. 55, No. 7, 2080–2087, Jul. 2007.
12. Conway, G. A. and W. G. Scanlon, "Antennas for over-body-surface communications at 2.45 GHz," *IEEE Trans. Antennas and Propagation*, Vol. 57, No. 4, 844–855, Apr. 2009.
13. Simunic, D. and M. Djurek "Electromagnetic dosimetry issues related to human exposure from body area networks devices," *Proc. 2008 International Symposium on Applied Sciences on*

Biomedical and Communication Technology, 1–5, Oct. 2008.

14. King, R. W. P., S. Prasad, and B. H. Sandler, "Transponder antennas in and near a three-layered body," *IEEE Trans. Microwave Theory and Techniques*, Vol. 28, 586–596, Jun. 1980.
15. Lea, A., H. Ping, J. Ollikainen, and R. G. Vaughan, "Propagation between on-body antennas," *IEEE Trans. Antennas and Propagation*, Vol. 57, No. 11, 3619–3627, Nov. 2009.
16. Sasamori, T., M. Takahashi, and T. Uno, "Transmission mechanism of wearable device for on-body wireless communications," *IEEE Trans. Antennas and Propagation*, Vol. 57, No. 4, 936–942, Apr. 2009.
17. Paknys, R., "Reflection and transmission by reinforced concrete – Numerical and asymptotic analysis," *IEEE Trans. Antennas and Propagation*, Vol. 51, No. 10, 2852–2861, Oct. 2003.
18. Paknys, R. and D. R. Jackson, "The relation between creeping waves, leaky waves, and surface waves," *IEEE Trans. Antennas and Propagation*, Vol. 53, No. 3, 898–907, Mar. 2005.
19. Harrington, R. F., *Time-harmonic Electromagnetic Fields*, IEEE Press, New York, 2001.
20. Chew, W. C., *Waves and Fields in Inhomogeneous Media*, IEEE Press, New York, 1995.
21. Tai, C. T., *Dyadic Green Functions in Electromagnetic Fields* 2nd edition, IEEE Press, New York, 1993.
22. Felsen, L. B. and N. Marcuvitz, *Radiation and Scattering of Waves*, IEEE Press, New York, 1994.
23. "Human body dimensions data for ergonomic design," Report of National Institute of Bioscience and Human-technology, Vol. 2, No. 1, 83–84, 1994 (in Japanese).
24. Gabriel, S., R. W. Lau, and C. Gabriel, "The dielectric properties of biological tissues: II. Measurements in the frequency range 10 Hz to 20 GHz," *Physics in Medicine and Biology*, Vol. 41, 2251–2269, 1996.
25. Mathews, J. H. and K. K. Fink, *Numerical Methods Using Matlab*, 4th edition, Prentice-Hall Inc., New Jersey, 2004.